A generalised mechano-kinetic model for use in multiscale simulation protocols

Benjamin S. Hanson[1], Lorna Dougan[1,2], Sarah A. Harris[1,2], Daniel J. Read[3*],

1 School of Physics & Astronomy, University of Leeds, Leeds, United Kingdom
2 Astbury Centre for Structural Molecular Biology, University of Leeds, Leeds, United Kingdom
3 School of Mathematics, University of Leeds, Leeds, United Kingdom

* d.j.read@leeds.ac.uk

Abstract

Many biophysical systems and proteins undergo mesoscopic conformational changes in order to perform their biological function. However, these conformational changes often result from a cascade of atomistic interactions within a much larger overall object. For simulations of such systems, the computational cost of retaining high-resolution structural and dynamical information whilst at the same time observing large scale motions over long times is high. Furthermore, this cost is only going to increase as ever larger biological objects are observed experimentally at high resolution.

We derive a generalised mechano-kinetic simulation framework which aims to compensate for these disparate time scales, capable of dynamically exploring a defined mechanical energy landscape whilst at the same time performing kinetic transitions between discretely defined states. With insight from the theory of Markov state models and transition state theory, the framework models continuous dynamical motion at coarse-grained length scales whilst simultaneously including fine-detail, chemical reactions or conformational changes implicitly using a kinetic model. The kinetic model is coupled to the dynamic model in a highly generalised manner, such that kinetic transition rates are continuously modulated by the dynamic simulation. Further, it can be applied to any defined continuous energy landscape, and hence, any existing dynamic simulation framework. We present a series of analytical examples to validate the framework, and showcase its capabilities for studying more complex systems by simulating protein unfolding via single-molecule force spectroscopy on an atomic force microscope.

Author summary

Our intention with this work is to provide a generalised, highly coarse-grained model to allow kinetic processes (conformational changes, protein unfolding, chemical reactions etc) to occur within the context of a dynamic simulation. Performing computationally intensive dynamic simulations to obtain kinetic information can be unjustifiably costly and scientifically inefficient, and so we instead want to emphasise that experimentally available kinetic information can be used to infer the underlying dynamics they result from. We hope our work can begin a discussion on the topic of computationally efficient science, and continue the drive towards collaborative science between theory and experimentation.

Introduction

Over the past decade, experimental techniques have matured to such an extent that we can observe biological systems on length scales never before seen. Cryo-electron microscopy is enabling us to determine the atomistic structures of macromolecular complexes without the need for crystallisation, providing us with significantly more realistic instances of biological functional pathways [1–3]. Additionally, the continued development of various forms of super resolution microscopy and high throughput data analysis allow us to observe motions over ever shorter time scales [4, 5]. Many of these structures are being deposited into the Electron Microscopy Data Bank (EMDB), which has seen an almost exponential growth rate over the past decade [6]. Simulation techniques are being developed which utilise this data, especially at coarse-grained scales [7]. However, further consideration is needed with respect to the meaning of physical models at these newly explored spatio-temporal scales [8], and to the practicalities of performing computer simulations of these almost microscopic objects.

We may take as an illustrative example the molecular motor dynein, a system we have previously investigate [9, 10]. We consider that the features we outline now for dynein are common to many biomolecules and the attempts to capture their operation in a multiscale simulation framework. Hanson *et al.* recently used existing all-atom molecular dynamics simulations of a single monomer of the motor to parameterise a much coarser continuum mechanical model of the same object [10], and found that a significantly coarser model can be used successfully for simulating the equilibrium dynamics. However, the biological function of the motor is in its so-called "powerstroke", a change of equilibrium shape driven by cascading atomistic processes [11] which generates the directed force required for the motor to do the useful physical work [12–14]. Experiments show that the time between individual powerstroke events is typically much longer than either the mechanical relaxation time of the molecule or the time over which the powerstroke itself occurs. Hence the change in equilibrium configuration associated with the powerstroke is often considered as an effectively instantaneous chemical kinetic event [15]. However, given that the underlying structure of the motor [10] and its physical environment [9] affect its equilibrium, these kinetic events may not be completely independent of the underlying dynamics from which the emerge. The question then arises as to how one should include the powerstroke event into coarse-grained dynamical models of dynein, and reconcile these disparate timescales.

Dynein is not the only example of such disparate timescales in biological physics. We believe that the issues encountered above are sufficiently general to warrant consideration. Any coarse-grained biomolecular simulation might need to model transitions between different states, in which the configuration of a molecule at mechanical equilibrium is changed. Two particular examples of this are (i) molecular motors (as in dynein above) in which the configurational change between pre- and post-powerstroke states is driven by reactions within chemical-kinetic cycle, or (ii) protein unfolding, either at equilibrium [16–18] or driven by application of external force. External force can play a role in both of these examples. Translational molecular motors such as dynein have measurable stall forces [14, 19], and these forces can be applied by other molecular motors acting in the opposite direction [20]. Proteins are subjected to large forces in the artificial setting of single-molecule force spectroscopy experiments using an atomic force microscope (SMFS-AFM), but also in natural settings such as titin within muscle fibres [21], and engineered biological matrices such as protein hydrogels [22]. These external factors change the effective activation energy of the kinetic transition, and hence change the rate and manner by which thermal fluctuations and other dynamical effects drive transitions in these types of system.

The above discussion shows a need for a framework in which the disparity between

dynamic and kinetic timescales are somehow reconciled, and their coupling explicitly modelled. This has been previously attempted specifically with respect to both molecular motors [23, 24] and much more commonly to protein unfolding [18, 25–30], but to our knowledge, a fully general approach has yet to be discussed. To address this considerable challenge in mesoscale modelling, we have developed a generalised 'mechano-kinetic' simulation framework which utilises both explicit mechanical modelling at mesoscopic length scales, whilst at the same time accounting for chemical-kinetic events beyond the scope of the dynamic model with a coupled kinetic model similar to a Markov state model. This coupling is such that the kinetic rates themselves dynamically alter as the system moves through the dynamic energy landscape and hence, using only the principle of detailed balance, our simulation framework enables the mesoscopic dynamical simulation to instantaneously contribute towards kinetic events such as conformational changes and chemical reactions, and thus implicitly affect dynamics at smaller length scales and vice versa.

Theoretical Development

Our goal is to derive a 'mechano-kinetic' simulation framework; a simulation that is able to dynamically explore a defined mechanical energy landscape whilst at the same time perform kinetic transitions between discretely defined states. Here, and in what follows, we use the word *dynamics* to refer to changes in shape and conformation of a molecule as it explores a mechanical energy landscape; we use the word *kinetics* to refer to (discrete) changes of state which would alter that landscape (e.g. due to a chemical change such as a binding or unbinding event). We recognise it is usually not possible to cleanly distinguish these. Nevertheless, such a distinction is forced on us in coarse-grained modelling: "dynamical" changes refer to changes in molecular configuration explicitly resolved in the model, whilst "kinetic" changes are driven by processes at smaller, unresolved, scales.

Mesostates

Importantly, we want the location in dynamical phase space to affect the kinetic processes in a thermodynamically consistent manner, such that we gain insight into how kinetic processes interact with different mechanical energy environments. To emphasise the target application of the biological mesoscale, and also to distinguish the discrete kinetic regime from continuous mechanical regime, we will refer to the discrete kinetic states as "mesostates".

Fig.1 shows a schematic of a kinetic network, where each mesostate has some associated occupation probability P_i. For a physical system, these occupation probabilities can be written in terms of a free energy, F_i

$$P_i = \frac{1}{Z_T} \exp\left(-\frac{F_i}{k_B T}\right), \tag{1}$$

where Z_T is the total partition function of the entire network, here acting as a normalisation constant. These probabilities, at equilibrium, must be related to the transition rates between mesostates, R_{ij} by the principle of detailed balance

$$R_{ij} P_i = R_{ji} P_j. \tag{2}$$

In principle, these probabilites and rates can be measured, either by experimentation or by a Markov State Model (MSM) calculation from a higher resolution simulation.

Microstates and Free Energy

As shown for mesostates 2 and 3 in Fig.1, each mesostate contains within it a (potentially large number) of microstates. What these microstates are, and how they are parameterised, will depend on the system in question. In the examples considered here, the microstates are considered to be the set of (mechanical) shapes or configurations that a protein can take: we denote the microstate by the multidimensional vector $\vec{x}$. So, our physical picture is that the molecule exists within some mesostate i for some time, dynamically exploring changes of shape represented by changes in $\vec{x}$.

The total partition function for the system is:

$$Z_T = \sum_i \exp\left(-\frac{F_i}{k_B T}\right) = \sum_i Z_i, \tag{3}$$

where the partition function for mesostate i is:

$$Z_i = \int_\Omega d\vec{x} g_i \exp\left(-\frac{E_i(\vec{x})}{k_B T}\right). \tag{4}$$

Here, $E_i(\vec{x})$ is the energy as a function of $\vec{x}$ (free energy if $\vec{x}$ are coarse-grained variables) and g_i is the (typical) density of states within mesostate i. Any dependence of density of state on $\vec{x}$ can be included as an entropic term within $E_i(\vec{x})$ (and should be, since it will affect the dynamics of $\vec{x}$). Then, the equilibrium probability density of system being at microstate $\vec{x}$ within mesostate i is:

$$p_i(\vec{x}) = \frac{g_i \exp\left(-\frac{E_i(\vec{x})}{k_B T}\right)}{Z_T}, \tag{5}$$

and $P_i = \int_\Omega d\vec{x} p_i(\vec{x})$. All dynamics and kinetics in the system must be consistent with these equilibrium distributions.

Kinetic transitions between microstates

At some instant, a kinetic event may occur such that the molecule transitions from mesostate i to mesostate j. But, that transition must actually occur from a microstate within i, to a microstate within j, as illustrated explicitly for mesostates 2 and 3 in Fig.1. Detailed balance must also apply to such transitions between microstates.

We define $r_{ij}\left(\vec{x}, \vec{x}'\right)$ to be the transition rate from a single microstate at $\vec{x}$ within i to a single microstate at $\vec{x}'$ within j. Then, the equilibrium rate of transition from volume $d\vec{x}$ to volume $d\vec{x}'$ is the probability of being in $d\vec{x}$, multiplied by the rate of transition per state, multiplied by the number of states in $d\vec{x}'$:

$$p_i(\vec{x}) d\vec{x} \times r_{ij}\left(\vec{x}, \vec{x}'\right) \times g_j d\vec{x}'.$$

A similar equation applies to the equilibrium rate of reverse transition from $d\vec{x}'$ to volume $d\vec{x}$, and hence (equating these two rates) we recover the expected detailed balance condition:

$$\frac{r_{ij}\left(\vec{x}, \vec{x}'\right)}{r_{ji}\left(\vec{x}', \vec{x}\right)} = \exp\left(-\frac{\Delta E_{ij}\left(\vec{x}, \vec{x}'\right)}{k_B T}\right), \tag{6}$$

where $\Delta E_{ij}\left(\vec{x}, \vec{x}'\right) = E_j\left(\vec{x}'\right) - E_i\left(\vec{x}\right)$.

Then, the total equilibrium rate of transition from mesostate i to mesostate j is obtained by integrating over all such pairs of volumes:

$$P_i R_{ij} = \int_\Omega d\vec{x} \int_{\Omega'} d\vec{x}' p_i(\vec{x}) g_j r_{ij}\left(\vec{x}, \vec{x}'\right). \tag{7}$$

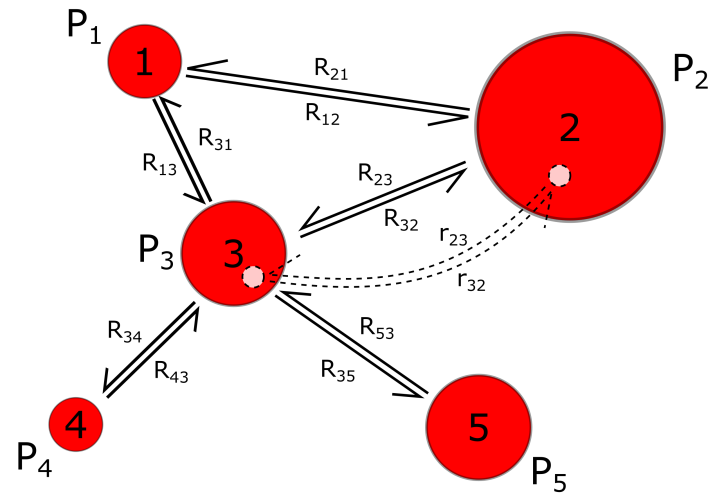

Fig 1. A dimensionless representation of a kinetic network with the number of states $N = 5$. Each state has an associated probability P_i which is determined by the number of available microstates within it. Transitions between states occur explicitly between microstates with rates r_{ij}, as shown by the dashed arrows, which then determine the relative transition rates R_{ij} between each pair of states i, j, as given by the principle of detailed balance.

A similar equation applies to the reverse transition rate $P_j R_{ji}$. Applying Eq.6 thus ensures that Eq.2 is fulfilled. Eq.7 is useful in that it relates transition rates between microstates, $r_{ij}\left(\vec{x}, \vec{x}'\right)$, to the total transition rate between mesostates R_{ij}.

A special case of the above is where the spaces $\vec{x}$ and $\vec{x}'$ are identical, density of states $g_i = g_j = g$, and transitions occur only between the same point in phase space, i.e. $\vec{x}' = \vec{x}$ for all transitions. In this case we may write:

$$r_{ij}\left(\vec{x}, \vec{x}'\right) = \frac{\widetilde{r}_{ij}\left(\vec{x}\right)}{g} \delta\left(\vec{x} - \vec{x}'\right).$$

Then the microscopic detailed balance becomes:

$$\frac{\widetilde{r}_{ij}\left(\vec{x}\right)}{\widetilde{r}_{ji}\left(\vec{x}\right)} = \exp\left(-\frac{\Delta E_{ij}\left(\vec{x}\right)}{k_B T}\right), \tag{8}$$

and Eq.7 simplifies as may be expected:

$$P_i R_{ij} = \int_{\Omega} d\vec{x} p_i(\vec{x}) \widetilde{r}_{ij}\left(\vec{x}\right). \tag{9}$$

All the specific examples pursued in this paper are of this simpler form. The more general Eq.7 becomes necessary if transitions occur between different points of phase space within mesostates i and j, or if the phase spaces of i and j are not identical. The former may occur, for example, in models where a dynamic transition through phase space is explicitly defined as a part of a kinetic transition, and the latter in coarse grained modelling where the two mesostates are represented by different coarse grained models.

The above equations are extremely general. They relate forward and reverse transition rates (via detailed balance), and mesoscopic transition rates to microsopic transition rates. These equations place constraints on what is "allowed" in a model. However, they are not sufficient to fully constrain a model: one needs to make further physical assumptions. In what follows, we explore some possible assumptions that are consistent with the preceding work.

Candidate microscopic models

We find it convenient to separate the energy of a microstate as $E_i(\vec{x}) = E_i^c + E_i^m(\vec{x})$, where $E_i^m(\vec{x})$ is the "mechanical" energy used to compute dynamics of $\vec{x}$ within mesostate i, and E_i^c represents all other contributions to the (free) energy of mesostate i that are independent of $\vec{x}$. Correspondingly, energy differences can be written as $\Delta E_{ij}(\vec{x}) = \Delta E_{ij}^c + \Delta E_{ij}^m(\vec{x})$.

This then allows us to write Eq.8 in the form

$$\frac{\widetilde{r}_{ij}\left(\vec{x}\right)}{\widetilde{r}_{ji}\left(\vec{x}\right)} = \frac{r_{ij}^c}{r_{ji}^c} \exp\left(-\frac{\Delta E_{ij}^m\left(\vec{x}\right)}{k_B T}\right) \tag{10}$$

where the 'intrinsic' rates r_{ij}^c are related as

$$\frac{r_{ij}^c}{r_{ji}^c} = \exp\left(-\frac{\Delta E_{ij}^c}{k_B T}\right). \tag{11}$$

We note that these intrinsic rates are not necessarily independent of $\vec{x}$: it may be, for example, that transitions are only possible within some region of phase space. However, their ratio is independent of $\vec{x}$. For the purposes of this work we will assume them to be constant, but recognise that so long as Eq.11 is satisfied, they can take any functional form.

We now indicate two candidate forms of model that are consistent with Eq.10.

1. **Mechanical energy difference model.** With insight from the work of Sarlah and Vilfan [23, 24], we separate the detailed balance condition of Eq.10 into individual rates as

$$\widetilde{r}_{ij}\left(\vec{x}\right) = r_{ij}^c \exp\left(-\frac{f_{ij}^m \Delta E_{ij}^m\left(\vec{x}\right)}{k_B T}\right). \tag{12}$$

   The factor f_{ij}^m indicates the fraction of the mechanical energy difference $E_{ij}^m\left(\vec{x}\right)$ that influences the forward transition rate $\widetilde{r}_{ij}\left(\vec{x}\right)$, the remainder being attributed to the reverse transition. Eq.10 then requires the constraint $f_{ij}^m + f_{ji}^m = 1$. The implicit assumption is of an energy barrier to the transition, located at some position along the reaction co-ordinate between mesostates i and j. The mechanical energy alters the height of that barrier in an Arrhenius-like fashion. $f_{ij}^m = 1$ suggests the barrier is located close to state j along the reaction co-ordinate, whilst $f_{ij}^m = 0$ indicates the barrier is close to i.

   We can now relate Eq.12 to equilibrium transition rates at the mesoscale. Substitution into Eq.9, and using Eqs.1 and 5 with $g_i = g$ gives

$$R_{ij} = \frac{\int_\Omega d\vec{x} r_{ij}^c \exp\left(-\frac{f_{ij}^m \Delta E_{ij}^m(\vec{x})}{k_B T}\right) \exp\left(-\frac{E_i(\vec{x})}{k_B T}\right)}{\int_\Omega d\vec{x} \exp\left(-\frac{E_i(\vec{x})}{k_B T}\right)}, \tag{13}$$

   and, with the assumption of constant r_{ij}^c, we finally obtain

$$R_{ij} = r_{ij}^c \frac{\int_\Omega d\vec{x} \exp\left(-\frac{f_{ji}^m E_i^m(\vec{x}) + f_{ij}^m E_j^m\left(\vec{x}'\right)}{k_B T}\right)}{\int_\Omega d\vec{x} \exp\left(-\frac{E_i^m(\vec{x})}{k_B T}\right)}. \tag{14}$$

   This equation determines the value of r_{ij}^c required in the model to obtain a given value of R_{ij} when the system is at thermal equilibrium. So, for example, R_{ij} may be an experimentally observed transition rate between two mesostates. Having

now determined the appropriate choice of r_{ij}^c, we can continue to use Eq.12, for example in a non-equilibrium situation where an additional external force is applied to the system, which would then result in a change in the overall average transition rate.

2. **Force-driven transition model.** A reasonable assumption in some situations is to consider that the transition rate from i to j is driven by some component of a force $f_i(\vec{x})$, which depends upon the configuration $\vec{x}$. So, for example, $f_i(\vec{x})$ could be a force acting across a bond, which may dissociate to drive a change of state (e.g. a protein unfolding). This force might (in many cases) be obtained from the gradient of the mechanical energy $E_i^m(\vec{x})$ with respect to one of the components of $\vec{x}$. This distinguishes the force-driven transition from the mechanical energy difference model (where the transition rate is related only to the difference in energy between mesostate i and j rather than gradient of the mechanical energy within a mesostate). Models explicitly considering external force have long been used ubiquitously, yet often in isolation, at the free-energy level [31].

   If the critical extension of the bond for dissociation is a small distance b, where $b = b_{ij} = b_{ji}$, the energy barrier towards the transition is then reduced by $f_i(\vec{x})b_{ij}$ giving transition rate:

$$\widetilde{r}_{ij}(\vec{x}) = r_{ij}^c \exp\left(\frac{f_i(\vec{x})b_{ij}}{k_B T}\right). \tag{15}$$

   It may be that the rate of the reverse transition is negligible and can be ignored. However, if re-association is to be considered a possibility then Eq.10 requires that:

$$\widetilde{r}_{ji}(\vec{x}) = r_{ji}^c \exp\left(\frac{f_i(\vec{x})b_{ij}}{k_B T}\right) \exp\left(-\frac{\Delta E_{ji}^m(\vec{x})}{k_B T}\right). \tag{16}$$

   We can again relate these microscopic transition rates to equilibrium transition rates at the mesoscale. Substitution into Eq.9, and using Eqs.1 and 5 with $g_i = g$ gives, for the forward rates:

$$R_{ij} = r_{ij}^c \frac{\int_\Omega d\vec{x} \exp\left(-\frac{E_i^m(\vec{x}) - f_i(\vec{x})b_{ij}}{k_B T}\right)}{\int_\Omega d\vec{x} \exp\left(-\frac{E_i^m(\vec{x})}{k_B T}\right)}. \tag{17}$$

   However, for the reverse rates:

$$R_{ji} = r_{ji}^c \frac{\int_\Omega d\vec{x} \exp\left(-\frac{E_i^m(\vec{x}) - f_i(\vec{x})b_{ij}}{k_B T}\right)}{\int_\Omega d\vec{x} \exp\left(-\frac{E_j^m(\vec{x})}{k_B T}\right)}. \tag{18}$$

   In an unbinding transition, for which this model is most appropriate, it would typically be the case that mesostate i (representing bound state) would be mechanically stiffer than mesostate j. Hence, integrals over $\exp\left(-E_j^m(\vec{x})/k_B T\right)$ are dominated by relatively small region of phase space V_i, whilst integrals over $\exp\left(-E_j^m(\vec{x})/k_B T\right)$ are dominated by a larger region of phase space $V_j \gg V_i$. Thus, the reverse transition rate in Eq. 18 contains an implicit factor of V_i/V_j, representing the fact that rebinding can only occur from state j to state i if the system is found in the correct region of phase space, close to the favourable region for state i. If $V_j \gg V_i$ then such occasions will be rare, through random thermal fluctuation.

   We note here that the factor $f_i(\vec{x})b$ occurring in these equations is a linearised energy contribution, which will typically only be appropriate in the region V_i of

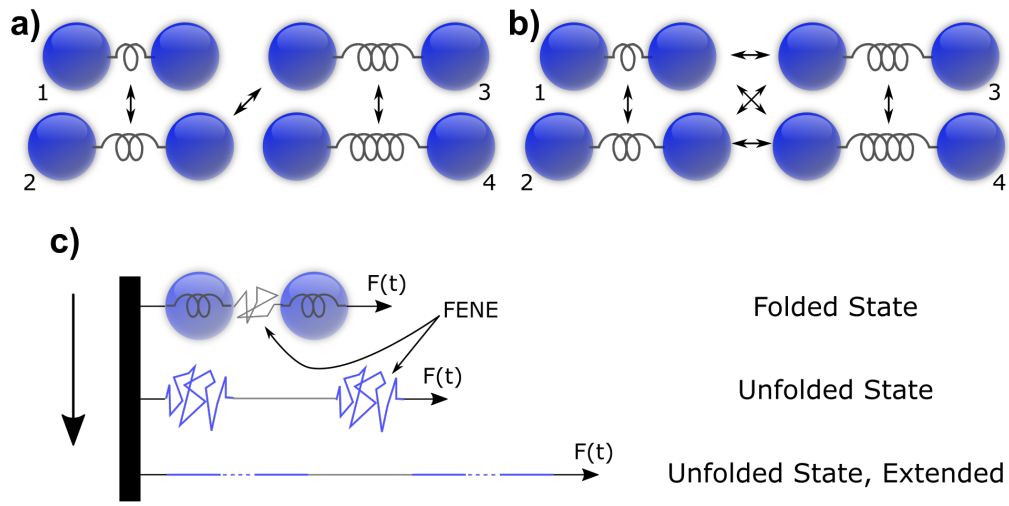

Fig 2. The structural models in each of our example systems. **a)** Four mesostates, defined by their different equilibrium lengths and spring constants. There is only a single transition pathway from mesostate 1 to mesostate 4, representing a process akin to (but distinct from) a reaction co-ordinate. **b)** Similar systems to the previous example, but this time every possible kinetic transition is allowed. **c)** By representing "proteins" as Hookean springs which can transition to springs with a modified finitely extensible non-linear elastic (FENE) potential, i.e. a polypeptide chain [32], we obtain a representation of protein unfolding by mimicking SMFS-AFM experiments.

phase space where mesostate i undergoes typical fluctuations. It may be that it is appropriate to set r^c_{ij} and r^c_{ji} to zero outside this region (and taking it back inside the integrals), so as to prevent the factor $f_i(\vec{x})b$ in equations 17 and 18 from creating spurious, unphysical effects.

The following section contains various examples which show the capabilities of the method, and hint at its generality and wide field of potential applicability.

Results

Fig.2 shows the various systems investigated in this section. Before discussion of those, however, we begin by showing how Eq.14 can be calculated for a specific system, and how Eq.12 is applied as part of a dynamic simulation protocol. This is done using the mechanical energy difference model, although an equivalent set of calculations could be performed for the force-driven transition model using Eqs.15-18.

Applying the mechano-kinetic framework

To investigate our model capabilities, we begin with a simple 1D dumbbell model; two beads of radius R connected by a Hookean spring with spring constant k_i and equilibrium length l_i. The dynamic simulation framework we use is a Brownian dynamics protocol, numerical integration of the Langevin equation where inertia, and hence velocity degrees of freedom, are neglected. For the two dumbbell coordinates x_1 and x_2, our Langevin equations are

$$\lambda \frac{\partial x_1}{\partial t} + k_i \left((x_2 - x_1) - l_i \right) = f_1^n(t), \tag{19}$$

$$\lambda \frac{\partial x_2}{\partial t} - k_i \left((x_2 - x_1) - l_i \right) = f_2^n(t) \tag{20}$$

Each bead is subject to a Stokes drag λ and as associated stochastic thermal noise f^n calculated via the fluctuation-dissipation theorem. The corresponding mechanical energy for the system is given by

$$E_i^m = \frac{1}{2} k_i \left(x - l_i \right)^2 , \tag{21}$$

where $x = x_2 - x_1$ defines the single elastic degree of freedom within the system.

The kinetic simulation component utilises the sets of internal spring parameters, k_i and l_i. These two parameters define the mesostate, i.e. k_i and l_i are the parameters for mesostate i, and will vary between mesostates. When altered, these parameters change the energy landscape independently of the location of the dumbbell nodes within phase space, setting $x = x'$ in Eq.14. In principle all parameters could vary between mesostates, but for clarity we consider only kinetic alterations in the elastic energy landscape. Hence, $R = 1\text{nm}$, $\lambda = 6\pi\text{Pa.s}$ and these remain constant across all mesostates.

With these independent definitions of the dynamic and kinetic simulation components, we can now couple them together. For this 1D system and in the absence of intertia, the mechanical energy term within Eq.14 is greatly simplified. Introducing Eq.21 into Eq.14 and expressing the denominator integral exponent as a polynomial in x gives only Gaussian integrals in x and so can be solved exactly, yielding

$$R_{ij} = r_{ij}^c \frac{1}{\sqrt{1 + f_{ij}^m \left(\frac{k_j}{k_i} - 1 \right)}} \exp \left(- \frac{f_{ij}^m \left(1 - f_{ij}^m \right) k_j \left(l_i - l_j \right)^2}{2 k_B T \left(1 + f_{ij}^m \left(\frac{k_j}{k_i} - 1 \right) \right)} \right) , \tag{22}$$

Eq.22 completes the coupling between dynamic and kinetic simulation components within our mechano-kinetic framework. From a set of R_{ij} together with our dynamic model, we can calculate the set r_{ij}^c. Now, following each dynamic simulation timestep, we include the probability of a mesostate transition as per Eq.12, where we convert the rates to transition probabilities by multiplying by the simulation timestep. Eq.12 therefore makes these transition probabilities explicitly dependent on the current microstate mechanical energy. If a transition occurs, we keep the two node positions constant, change the spring parameters, and allow the dynamic simulation to continue.

A small aside, the introduction of instantaneous kinetic transitions within a dynamic simulation introduces another timescale related to numerical accuracy and statistical equilibration, the derivation of which is provided in Supporting Information along with physical validation of each simulation component.

A four-state system

To investigate the behaviour of our model when applied to a molecule undergoing conformational changes, we have designed a series of kinetic transitions using the dumbbell model corresponding to a four state system, in which the average length of the dumbbell increases throught the states. We define two alternative systems of this set of kinetic mesostates, given by their mechanical parameterisations in Table 1, together with an associated equilibrium kinetic transition rate matrix corresponding to both systems given in Table 2. The schematic of this system is shown in Fig.2a.

As Table 2 defines all of the expected transition rates, which in principle may have been experimentally measured, it also implicitly defines the mesoscale free energy landscape and all of the resultant occupation probabilities. Thus our investigation will

Mesostate (i)	k_i (pN/nm)	l_i(nm)
1	10	1
2	10	2
3	10	3
4	10	4

Mesostate (i)	k_i (pN/nm)	l_i(nm)
1	200	1
2	50	2
3	50	3
4	200	4

Table 1. The two families of material parameters used to define the mesostates in the four-state kinetic networks of the dumbbell model. The first (left) set contains equal and relatively low values of k_i whereas the second (right) set of k_i are much higher. The values of l_i linearly increase with the mesostate index.

Transition Rates, R_{ij} (μs^{-1})					P_i
From / To	1	2	3	4	
1	N/A	0.916	-	-	0.013
2	0.337	N/A	50	-	0.035
3	-	6.767	N/A	18.394	0.256
4	-	-	6.767	N/A	0.696

Table 2. The average transition rates between mesostates used in the four-state kinetic networks of the dumbbell model. The mesostate occupation probabilities have been analytically calculated for comparison with simulation.

tell us nothing new at the mesoscale level at this stage. Instead, our aim is to analyse the modifications to the kinetic rates made by the continuous underlying dynamics, and verify that the measured, average kinetic behaviour is reproduced. Note that many of the transition rates shown in Table 2 are zero, indicating that direct transitions cannot occur between these states. However, transitions via other intermediate states can still occur (i.e. from mesostate 1 to mesostate 3 via mesostate 2).

The energy landscapes implied by this kinetic system are illustrated in Fig.3. We see in Fig.3b that as all of the stiffness parameters k_i are equal in the first parameterisation, no particular state is preferable over long periods of time with respect to mechanical energy. On the other hand, in the second parameterisation we include two high stiffness states (k_1 and k_4) and two low stiffness states (k_2 and k_3). However, irrespective of the mechanical energy environment, the free energy implied by the average rates, shown in Fig.3a as a function of some hypothetical 1D reaction co-ordinate, shows that we have implicitly included two free energy barriers, a metastable state and an overall difference in the free energy minima between the final state and the initial state. We emphasise that the "pseudo-reaction co-ordinate" is not the extension of the dumbbell, but some underlying variable which we have implicitly coarsened over to define our kinetic states. The shape of the curve in Fig.3a is implied by the mesostate transition rates, and the specific scale by the Arrhenius equation (see Eq.S2 in the Supporting Information). Finally, we set $f_{ij}^m = 0.5$ for all i, j.

Four state system - Results

For each mechanical simulation parameterisation, Table 3 shows the rates r_{ij}^c which are modified by exploration of the mechanical energy landscape to obtain the R_{ij} values shown in Table 2. Let us briefly investigate some of the properties of these values. For the set of r_{ij}^c where all the k_i are equal for the four mesostates, each r_{ij}^c is increased from its corresponding R_{ij} value by the same multiplicative factor. This is because the mechanical energy environments for each state are identical, albeit translated in space, and so with the application of Eq.22, all integral results are the same for every state pair. The presence of a mechanical energy landscape here, then, acts as a universal barrier to kinetic transition, such that an extra amount of energy is required to make

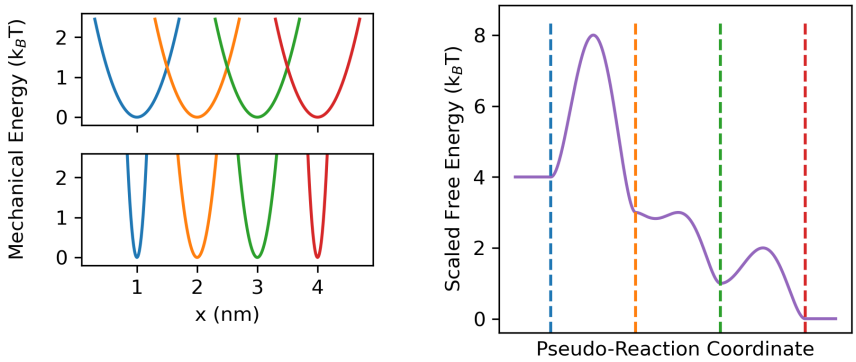

(a) **(b)**

Fig 3. The two "levels" of energy landscape within the four-state kinetic networks of the dumbbell model. a) The mechanical energy landscapes given in Table 1, where the occupation of each state is given a different colour. Top: Set 1 - All values of k_i are equal. Bottom: Set 2 - Values of k_i vary between mesostates. b) A possible representation of the free energy as a function of some hypothetical "pseudo-reaction co-ordinate", with barriers implied by the rates given in Table 2. The free energy scale was set arbitrarily by constraining Eq.S2. The "center" of each mesostate is shown as a vertical dashed line.

the kinetic transition. For the other set, corresponding to the mesostates with differing k_i values, we see a similar effect for r^c_{23} and r^c_{32} which, having the same mechanical energy landscape, are increased from their corresponding mesoscopic values by the same factor. The increase here is greater than in the previous (equal k_i) network, as the values of k_i are significantly higher. Importantly, because the values are increased by the same factor, the detailed balance condition between the pair of states is unchanged by the presence of a mechanical energy landscape and thus, while that rates are slower, the contributions to the equilibrium probabilities will be the same. However, this is not the case for any of the other pairs of rates in this network. As the mechanical energy environment changes between mesostates 1 & 2, and 3 & 4, the relative increase of r^c_{ij} from the associated R_{ij} value is different, showing that the detailed balance condition of the r^c_{ij} values are not the same as the mesoscopic R_{ij} values. In other words, dynamic motion through a mechanical energy landscape, in the general case, modifies the detailed balance conditions between the defined kinetic states.

Although the r^c_{ij} values calculated and used in each simulation are different, Table 4 shows the equilibrium mesostate occupation probabilities for both sets of mechanical material parameterisations, calculated by averaging the expected occupation probabilities from a single, long-time simulation over many repeats beginning in different initial states. We can see that the mesostate occupation probabilities for the two simulations are equivalent to the analytically calculated values given in Table 2, despite the large differences in the values of k_i. This clearly shows that the mesostate occupation probabilities within our model do indeed remain constant as required, being fixed by the pre-defined R_{ij} values, whilst the underlying mechanical energy landscape is modified.

Fig.4 shows the probability density of length fluctuations at equilibrium from a single simulation of each set of mesostates. We see that whilst the kinetic rate modifications within our model take the mechanical energies into account in order to return the average rates R_{ij}, the mechanical energy landscape is still fully realised within the framework. In particular, we see that the low mechanical stiffness of individual states in

Transition Rates, r^c_{ij} (μs^{-1})				
From / To	1	2	3	4
1	N/A	1.241	-	-
2	0.457	N/A	67.761	-
3	-	9.171	N/A	24.928
4	-	-	9.171	N/A

Transition Rates, r^c_{ij} (μs^{-1})				
From / To	1	2	3	4
1	N/A	8.239	-	-
2	6.063	N/A	228.56	-
3	-	30.934	N/A	330.91
4	-	-	60.869	N/A

Table 3. The instantaneous transition rates between mesostates used in the four-state kinetic networks of the dumbbell model corresponding to the two sets of mesostates given in Table 1. Top: Equal, low k_i mesostates. Bottom: Differing, large k_i values.

	Mesostate Occupation Probabilities, P_i			
Mesostate	1	2	3	4
Set 1	0.012(1)	0.034(1)	0.256(2)	0.698(2)
Set 2	0.014(1)	0.036(1)	0.258(2)	0.693(3)

Table 4. The final expected mesostate occupation probabilities within the four-state kinetic networks of the dumbbell model, which accurately reproduce the analytically calculated rates given in Table 2. Each set corresponds to a different set of material parameters as defined in Table 1. Uncertainties in the last digit are shown in brackets.

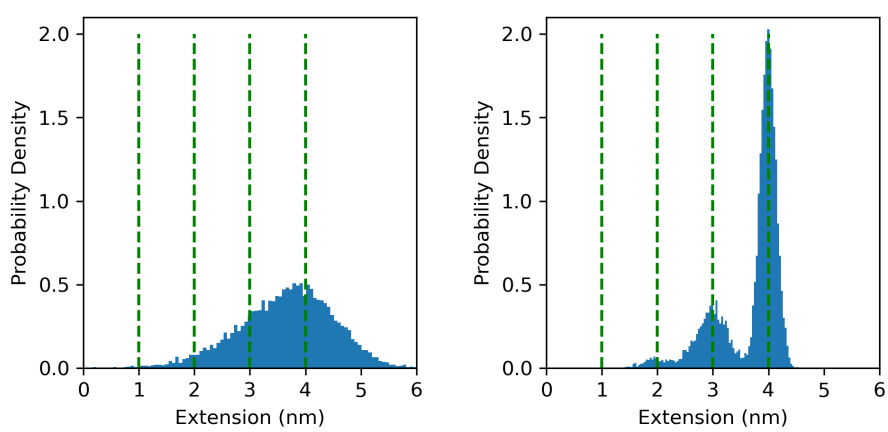

(a) **(b)**

Fig 4. The microstate probability densities from simulation of the four-state kinetic networks of the dumbbell model. The mechanical equilibrium positions corresponding to each state are shown as dashed green lines. a) Mesostate set 1 b) Mesostate set 2.

Fig.4a means that length fluctuations within each state are relatively large compared to the associated equilibrium lengths, resulting in a unimodal (albeit skewed) overall distribution centred around, but not exactly on, the most likely mesostate. Within a standard Markov state model, each of these states would likely be indistinguishable from one another, yet our implied knowledge of both the mesostate kinetics and mechanical energy landscape allows us to include them anyway, such that their indistinguishability is effectively a deduced property. On the other hand, for the second parameterisation in Fig.4b, the higher mechanical stiffness suppresses the length fluctuations within each mesostate so that the individual mesostates are distinguishable in the overall length distributions, with clear Gaussian distributions centered on each equilibrium length. This is less apparent for mesostates 1 and 2, however, as their associated free energies are significantly higher, and hence their occupation probabilities lower.

Overall we see that within the mechano-kinetic framework, no matter the structure of the mechanical energy landscape, the introduction of Eq.22 into Eq.12 enables the simulation to reproduce the R_{ij} values used as input parameters. As such, we have used the measured kinetic rates given in Table 2 together with the spring parameters in Table 1 to infer the specific form of the mechanical energy landscape. Further information on the interdependence of the kinetic and dynamic regimes with respect to the mechanical energy is given in Supporting Information. However, we will see in the next section that we can go further than the simple reproduction of existing measurements, and consider how direct external modifications to the mechanical energy landscape affect the resultant kinetic behaviour.

External Forces

We now investigate how our framework behaves when an external potential is added to the equilibrium system. As previously discussed, we may wish to determine the effect of applying external mechanical forces to biological objects such as proteins or molecular motors. Consider the case where either experiments or high-resolution simulations have been performed and both the free energy and mechanical energy landscapes of the object in isolation are well known. For the case of dynein, our illustrative system, both mechanical [33, 34] and kinetic [12, 35] information is available to parameterise the system. For proteins and unfolding in general, Hughes *et al.* provide a detailed review [32]. Using this information, we can use our mechano-kinetic simulation framework to make predictions base on these experimental systems.

To explore this type of problem in a general sense, we have designed two kinetic networks, both of which use the dumbbell model together with set of mesostates defined in Table 5. The first network is similar to the previous four-state example, whereas the second network is a fully connected kinetic network, where direct transitions between all states are possible. The schematic of this second system is shown in Fig.2d. The associated transition rates defining these networks are given in Table 6, left and right tables respectively. In contrast to the previous unforced four-state example, we here observe that because all of the rates are the same, when unperturbed, this system initially ought to have an equal probability of being in each of the mesostates. However, under the subsequent application of external forces we would expect the forces, as a source of mechanical energy, to bias the states in some manner. Within the *dynamic* simulation component, we apply a constant external force f^{ex} to both nodes of the dumbbell but in opposite directions, therefore biasing the dumbbell to higher extensions. To clarify, we use the values of r_{ij}^{c} as given at equilibrium in the absence of external forces, and modify the reaction rates via Eq.12 to account for additional contributions to the mechanical energy from the external forces. With this approach we are able to use our mechano-kinetic model to predict not only how the application of this external force within the dynamical simulation affects the overall kinetic transition rates between

Mesostate (i)	k_i (pN/nm)	l_i(nm)
1	25	1
2	25	2
3	25	3
4	25	4

Table 5. The material parameters used to define the mesostates used in the kinetic network of the dumbbell model with external forces applied.

Transition Rates, R_{ij} (μs^{-1})					P_i
From / To	1	2	3	4	
1	N/A	50	-	-	0.25
2	50	N/A	50	-	0.25
3	-	50	N/A	50	0.25
4	-	-	50	N/A	0.25
Transition Rates, R_{ij} (μs^{-1})					P_i
From / To	1	2	3	4	
1	N/A	16.6	16.6	16.6	0.25
2	16.6	N/A	16.6	16.6	0.25
3	16.6	16.6	N/A	16.6	0.25
4	16.6	16.6	16.6	N/A	0.25

Table 6. The matrices defining the two sets of average transition rates between mesostates, together with the expected mesostate occupation probabilities, used in the kinetic network of the dumbbell model with external forces applied. Top: A single path through the mesostate network. Bottom: A fully connected kinetic network. These rates were chosen such that the total rate of leaving any given mesostate is equivalent to that in the single pathway model.

mesostates, but also determine where those transitions are likely to occur in the mechanical energy landscape.

External Forces - Results

Fig.5 shows the steady state occupation probabilities of each mesostate as a function of applied force, for both sets of rates. These were calculated by averaging the expected occupation probabilities from a single, long-time simulation over three repeats, with each simulation beginning in mesostate 1 at mechanical equilibrium. Although all of the values of k_i in Table 5 and initial transition rates in Table 6 are equal, indicating no native energetic preference for any of the mesostates (as can be seen when zero external force is applied), the application of force immediately biases the system towards larger extensions. We also see that Figs.5a and 5b are almost identical. For each mesostate in ascending order, the root-mean-square deviations of the residuals of one graph with respect to the other are $0.006, 0.004, 0.006$ and 0.006 respectively. This indicates that the steady-state occupation probabilities as a function of applied force are independent of the connectivity of the kinetic network, but are rather given simply by the Boltzmann distribution, modified to account for the extra energy contribution from the externally applied force. Detailed balance implies that this change is brought about within the model via a change in the resulting values of R_{ij}, but key is that this is propagated from the dynamic component of the model into the kinetic component.

The application of force across all mesostates effectively generates an additional contribution to the free energy. As such, these forces can be included in pure kinetic models as free energies, ΔF_{ij}^{ex}, using a term such as $\Delta F_{ij}^{ex} = f^{ex}\Delta x_{ij}$ where Δx_{ij} is

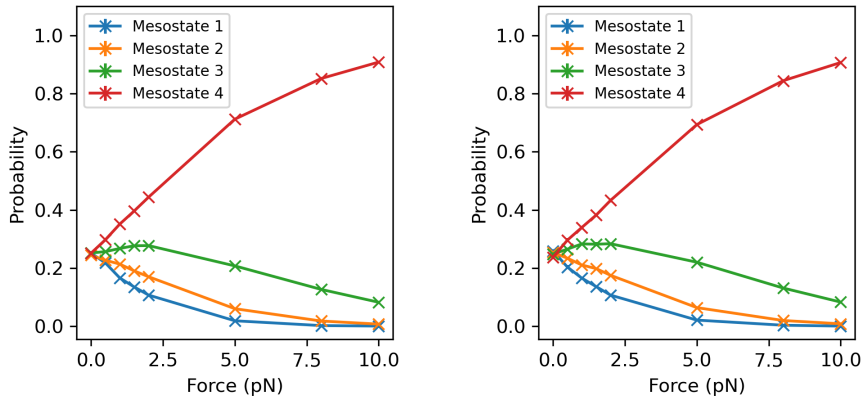

(a) **(b)**

Fig 5. The expected occupation probability of each mesostate of the dumbbell model as a function of applied force. a) The single pathway network. b) The fully connected network.

some approximation of the expected extension. This is similar to the force-driven transition model, except that the force is introduced at the kinetic (free-energy) level. However, with our explicit inclusion of the mechanical energy environment, we can observe the subtleties occurring at the microscale. Fig.6 shows the probability distributions, in the single pathway system, of dumbbell extension for zero external force and 10pN respectively, separated by mesostate. Overlapping these in a lighter colour are the distributions of dumbbell extension at the moment of transition into another mesostate. We see Gaussian distributions in the extensions, indicating thermodynamic equilibrium and reinforcing the results of Fig.5. In the Fig.6a transition distributions, we see either single or bimodal overlapping Gaussian distributions centred on the the half-way points between the each neighbouring pair of states, a direct consequence of the fact that the difference between two quadratic energy potentials is itself quadratic (see Supporting Information). Under external force, however, in Fig.6b, we observe all of these probability distributions have effectively been pulled over to higher extensions, with the bimodal distributions of mesostates 2 and 3 forming a single mode centred at higher extensions, and mesostate 1 having a much smaller occupation and number of transitions occurring.

Fig.7 shows the same information but for the fully connected network system. We observe approximately the same occupation probability distributions as in Fig.6, as may be expected from Fig.5, but our transition probability distributions are slightly more spread out. This is especially apparent if we compare mesostate 1 of Figs.6a and 7a, and mesostate 4, and is due to the fact that the fully connected network has more possible transition pathways. Indeed, as defined by our rates, mesostate 1 has an equal probability of transitioning straight to state 4 on average as it does mesostate 2. We therefore see that while the two systems shown yield the same occupation probabilities per mesostate, and change similarly under the application of force external to the initial parameterisation using Eq.22, the dynamical motion through phase space that we infer from the application of force at the continuous microstate level is dependent upon the structure and connectivity of the the kinetic landscape, i.e. which kinetic transitions are permitted.

The above is suggestive of alternative methods to parameterise the model from experiments. It may be the case that it is not possible to obtain R_{ij} from equilibrium experimentation (e.g. if the rates are too slow, or too fast). A viable alternative, then,

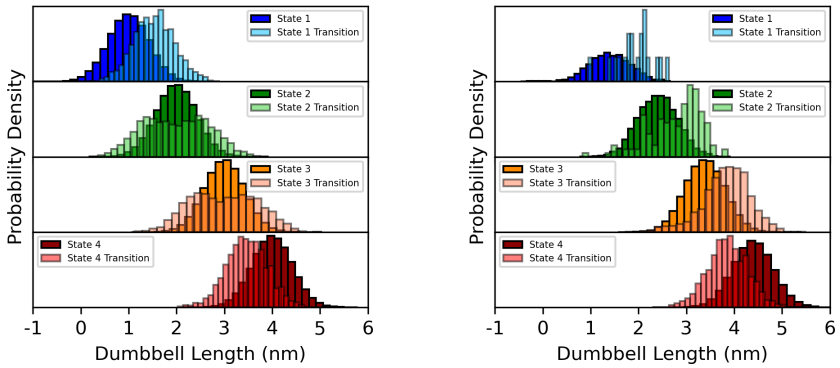

(a) **(b)**

Fig 6. The normalised probability distributions, in the single pathway system, of dumbbell node separation at the moment of transition into another mesostate. a) 0pN force applied. b) 10pN force applied.

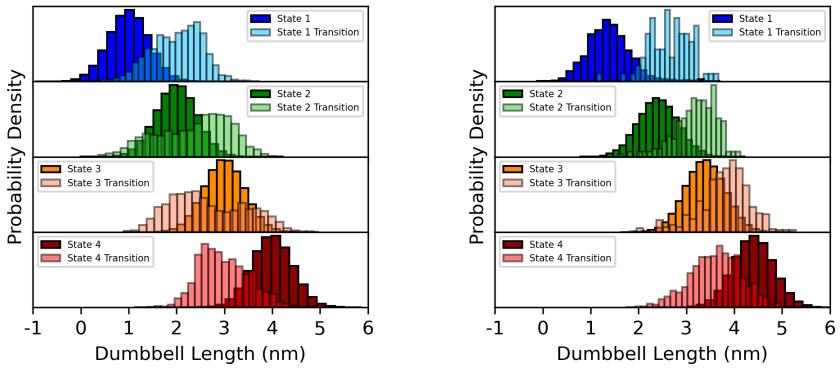

(a) **(b)**

Fig 7. The normalised probability distributions, in the single pathway system, of dumbbell node separation at the moment of transition into another mesostate. a) 0pN force applied. b) 10pN force applied.

is to measure transition rates accelerated under the application of external forces. Such forces modify the energy landscape, but if these modifications are included in 14 and used to derive an alternate version of Eq.22, then the necessary r_{ij}^c values can be obtained from the measured R_{ij} under external force. Then, on removal of the force from the model, the equilibrium R_{ij} (in the absence of force) may be inferred. This is a further example of how this mechano-kinetic framework can go beyond simply reproducing the initial parameterisation from experiment, extending the simulations to experimentally difficult and potentially infeasible scenarios for predictive purposes. The next section shows this formulation in the context of protein unfolding.

Protein Unfolding

We now apply our framework to the problem of protein unfolding by mimicking SMFS-AFM experiments on polyproteins. At the same time, we will use protein unfolding as an example problem to investigate the differences between the two types of microstate model discussed in the Theoretical Development Section: the mechanical energy difference model and the force-driven transition model. The schematic of this system, irrespective of kinetic model, is shown in Fig.2c. To model protein unfolding, we choose maltose binding protein (MBP) as a model protein. MBP was chosen due to the availability of all the required information for our model. Rief *et al.* have studied MBP in great detail using SMFS-AFM [36] and further, equilibrium mechanical properties have been measured to a high accuracy using elastic incoherent neutron scattering (EINS) [37]. In addition, equilibrium unfolding behaviour has been experimentally inferred by Na *et al.* [17]. Finally, MBP has recently been used in cross-lengthscale mechanical studies of globular protein-based hydrogels [22], and so our insights here may assist in the future understanding of unfolding in these systems.

We define a mesostate for both the folded and unfolded states of each protein. The folded state, being in 1D, can again be represented as a Hookean spring with an approximate spring constant $k_1 = 30.3$pN/nm [37] and equilibrium length $l_1 = 5nm$, approximately representing MBP [38]. The unfolded state can then be represented using a modified FENE potential, with associated force

$$\begin{cases} F = -k_2 \frac{x-l_2}{1-\left(\frac{x-l_2}{l_c}\right)^2} & x \leq x_{lim} \\ F = -k_{lim}(x - l_{lim}) & x > x_{lim}. \end{cases} \tag{23}$$

Eq.23 represents a non-interacting amino acid chain with only an entropic restoring force between the N- and C- termini at small extension. For $x \leq x_{lim}$, both the force and effective stiffness of the chain tend to infinity as $x - l_2 \to l_c$ as the amino acid chain straightens and the large enthalpic contributions become apparent. l_c, then, is the contour length of the polypeptide. This potential reproduces some of the core behaviour of the worm-like chain model, a more common model for polypeptides in used SMFS-AFM experiments [32]. Unfortunately, the effective linear stiffness tending to infinity presents significant numerical problems, severely limiting the integration timestep we can take at large extensions. To compensate for this, we define the effective linear stiffness at each x, k_{eff}, as

$$k_{eff}(x) = \frac{dF}{dx} = \frac{k_2}{1-\left(\frac{x-l_2}{l_c}\right)^2}\left(1 + \frac{2\left(\frac{x-l_2}{l_c}\right)^2}{1-\left(\frac{x-l_2}{l_c}\right)^2}\right). \tag{24}$$

We relax the infinite barrier in the standard FENE potential by choosing a value k_{lim}, such that when $k_{eff} > k_{lim}$, the potential becomes linear again with k_{lim} being the new

Structure	Mesostate (i)	Type	k_i (pN/nm)	l_i(nm)	l_c (nm)
Protein	1	Hookean	30.3	5	N/A
Protein	2	FENE	0.035	0	148
Linker	1	FENE	1.28	0	4.0

Table 7. The energy function and material parameters used to define the protein mesostates used in the kinetic network of the polyprotein unfolding model.

stiffness. This transition occurs at a value x_{lim}, and requires a new effective equilibrium length l_{lim}, both of which can be numerically calculated prior to the start of the simulation. We effectively use the FENE potential to transition from a linear stiffness k_2 to a maximum linear stiffness k_{lim}. We set $k_{lim} = 411$pN/nm so that for our chosen $k_BT = 4.11$pN.nm, fluctuations in the modified FENE chains are well-defined and negligible at large extension.

We connect five proteins in series with shorter segments of modified FENE potential amino-acid chain with only 1 mesostate defined, representing the linker domain of an engineered polyprotein [32]. We use five primarily because relatively short polyproteins have previously been under independent investigation by the authors [39–42]. FENE parameters were calculated by using the limiting, soft case of the WLC model together with the number of amino acids in each chain, assuming that the persistence length of the chain $L_p = 0.4$nm [43]. All parameters are given in Table 7.

The average kinetic rates R_{ij} in the absence of force are given in Table 8. The native unfolding rate of MBP was sourced from pulse proteolysis experiments [17], whereas the refolding rate was approximated using simple diffusion calculations i.e. the time taken for half the amino-acid chain to diffuse its own length. These rates were used with Eq.14, and the relevant integrals were calculated numerically to account for the more complex modified FENE potential.

Transition Rates, R_{ij} (μs^{-1})			P_i
From / To	1	2	
1	N/A	6×10^{-13}	~ 1
2	2.15×10^{-3}	N/A	~ 0

Table 8. The initial set of transition rates (in the absence of external force) used to investigate protein unfolding.

All protein unfolding simulations were performed by fixing the position of the left-most particle in our polyprotein and applying a force to the right-most particle in the $+x$ direction. This force progressively varies in a manner identical to the constant-velocity steered MD protocol implemented in the NAMD MD package. An analytical investigation of the behaviour of this model is given as Supporting Information.

Finally, when implementing the mechanical-energy difference model, we proceed as we have so far with the integrals in Eq.14 performed to determine each r^c_{ij}. For the force-driven transition model, we require an additional parameter b_{ij} for each integral in Eqs.17 and 18. Rather than parameterise from experimental data [36], we investigate the behaviour of this parameter as a part of the protein-unfolding simulation suite.

Protein Unfolding - Results

We begin our investigation with a brief investigation of the effect of thermal noise on the measured unfolding force of our proteins, implementing both the mechanical-energy difference (MED) model and the force-driven transition (FDT) model. Thermal fluctuations, while small in comparison to work done by the externally applied force, are

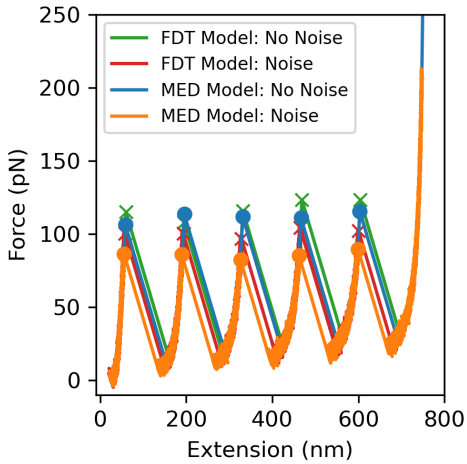

Fig 8. A pair of polyprotein unfolding curves from associated protein unfolding simulations showing how the presence of thermal noise affects the unfolding kinetics.

nevertheless included in the dynamic portion of the simulation, and therefore ought to directly affect the emergent kinetics. We set the stiffness of our constant-velocity spring component, $k_c = 1\text{pN/nm}$, and the pulling speed, $v_c = 5 \times 10^{-4}\text{nm/ns}$, to minimise the signal-noise ratio and at the same time increase the force at a reasonable rate in real time. In the FDT implementation, we set $b = 1\text{nm}$ for the unfolded protein, an arbitrary choice but of the correct order of magnitude for protein unfolding [39].

Fig.8 shows four characteristic SMFS-AFM curves extracted from mechano-kinetic simulations performed with and without thermal noise for both model implementations. We emphasise, the force measured here on the y-axis is the external tension within the simulated cantilever components, not the internal force within any of the subunits. The extension on the x-axis is measured from the N-terminus of the first monomer to the C-terminus of the last monomer, not the position of the cantilever component. This choice best represents what would be the tip of the cantilever in a real experiment.

We can see clearly that thermal noise has a significant effect on the unfolding force in both cases. By extracting the five peak forces (and their associated extensions), we can gain statistics for the unfolding kinetics. It has been previously observed that each specific peak has its own kinetic characteristics [44] but for now, we take the average of the these values from each simulation to gain single representative values for each system. For the MED model, in the absence of thermal noise, we measure an unfolding force, $F_{un} = 111.6 \pm 1.4\text{pN}$, and a peak-to-peak distance, $x_{pp} = 136.3 \pm 0.3\text{nm}$, and in the presence of thermal noise, we measure $F_{un} = 85.9 \pm 1.0\text{pN}$ and $x_{pp} = 135.9 \pm 0.7\text{nm}$. For the FDT model, in the absence of thermal noise, we measure an unfolding force, $F_{un} = 117.2 \pm 2.6\text{pN}$, and a peak-to-peak distance, $x_{pp} = 136.2 \pm 0.5\text{nm}$, and in the presence of thermal noise, we measure $F_{un} = 100.1 \pm 1.1\text{pN}$ and $x_{pp} = 135.9 \pm 0.3\text{nm}$. In all cases the measured x_{pp} value is similar, and the curves overlap well, implying physical consistency between simulations with and without noise. However, the measured x_{pp} values are lower than $l_c - (l_1 + F_{un}/k_1)$, which is the value we would expect if the FENE chain were to fully extend under the externally applied force. This implies that the proteins gain enough energy to unfold at slightly lower extensions. Nevertheless, this difference is relatively small. More importantly, the presence of thermal noise lowers the required unfolding force by approximately 25pN in the MED model, and 17pN in the FDT model. This difference in the reduction in F_{un} upon the inclusion of thermal noise is outside the uncertainty, suggesting a real difference

Parameter	Values			
k_1 (pN/nm)	10.0	30.3	50.0	
v_c (nm/ns)	5×10^{-4}	1×10^{-3}	5×10^{-3}	1×10^{-2}

Table 9. The parameter space investigated to determine the effect on the unfolding forces and peak-to-peak separations of protein unfolding curves.

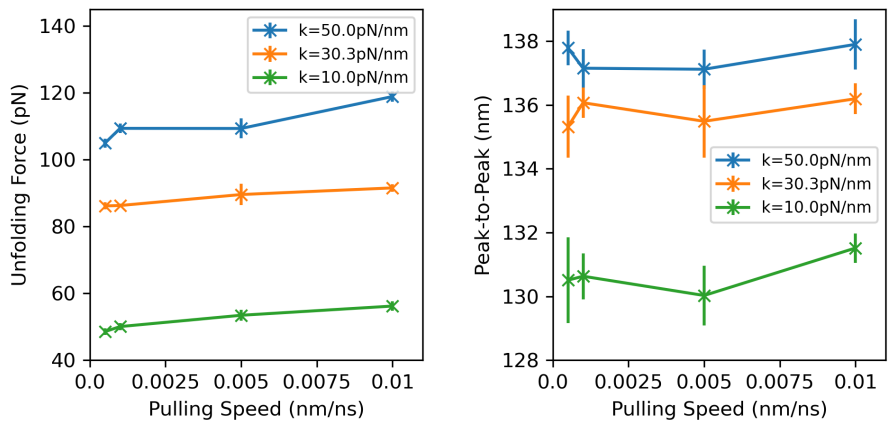

(a) **(b)**

Fig 9. A series of protein unfolding simulations showing how the cantilever pulling speed and protein stiffness affects the unfolding kinetics. a) Unfolding forces. b) Peak-to-peak distances.

between the models, but may be due to the difference in the value of b used and the average distance to the unfolding transition in the MED model. In both cases however, such a reduction in F_{un} was quite unexpected as thermal fluctuations contribute a modest $0.5k_BT$ of mechanical energy on average at zero external force, a negligible impact on the stability of most proteins, and MBP in particular. On reflection, however, due to the exponential nature of Boltzmann's equation, we see that the same amount of energy at high force has a relatively large impact, pushing the protein over the energy barrier required to unfold. This is a significant validation of the relevance of thermal noise in biological systems beyond being simply a tool for diffusion and entropic exploration of conformational space. This will be the case especially in non-equilibrium simulations and in models of proteins with low barriers to unfolding, such as intrinsically disordered proteins [45] and some extremophilic proteins [46–48]. All simulations from this point forward will be performed with thermal noise included.

We now investigate the effect on our system of variations in the (folded) protein spring constant k_1, and the pulling speed v_c, again implementing the mechanical-energy difference model. It is well known that changes in the pulling speed ought to alter the measured unfolding force due to the unfolding mechanism itself, but interestingly, West *et al.* also predicted that the existence of internal dynamics ought to alter the unfolding transition kinetics [26], and varying k_1 ought to allow a systematic analysis of this. We performed a single unfolding simulation for each of the parameter pairs defined in Table 9, and again extracted the unfolding forces, F_{un}, and and peak-to-peak distances, x_{pp}. All other parameters were kept constant between simulations, including the average rates R_{ij}.

From Fig.9, we observe that the internal mechanical stiffness has the most significant effect on both F_{un} and x_{pp} for all values of v_c (for a constant set R_{ij}). Rewriting the

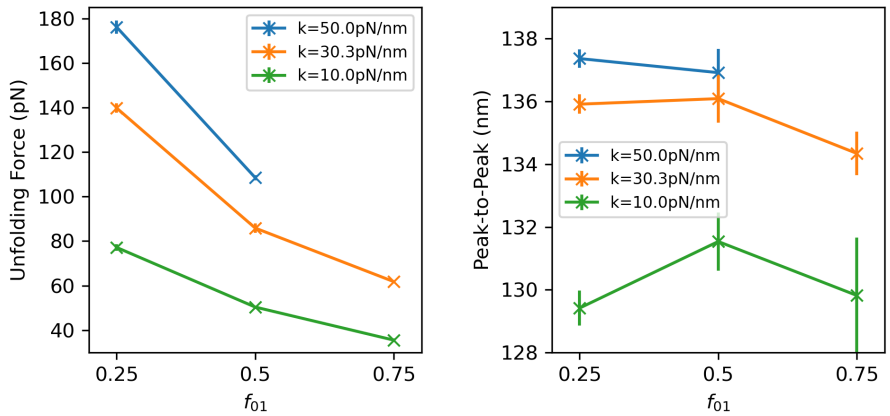

(a) **(b)**

Fig 10. A series of protein unfolding simulations, varying f_{ij} and k_1 a) Unfolding forces. b) Peak-to-peak distances.

linear protein energy explicitly in terms of force, $E = 0.5k_1(x - l_1)^2 = \frac{F^2}{2k_1}$, we see that for a higher stiffness, a higher force is required to reach the same energy. Thus, we see that the unfolding force increases with the internal stiffness of the protein. Interestingly, the peak-to-peak separation also increases with internal protein stiffness. As a function of the cantilever pulling speed v_c, however, we see too much variation between peak-to-peak values to draw any conclusions. However, it is clear that the unfolding force does slightly increase with v_c, as expected.

We will now use the protein unfolding simulations to investigate the effect of the set of f_{ij} in the mechanical-energy difference model. These values were (to our knowledge) first used conceptually by Sarlah *et al.* to imply a "mechanical activation energy", and modify how far towards the activation energy we need to be to perform the discretised kinetic transition [23]. In the Supporting Information, we show that this is indeed the case. Fig.10 shows the results of altering f_{ij} on the protein unfolding simulations with $k_1 = 30.3$ pN/nm and $v_c = 10^{-3}$nm/ns, where f_{01} on the x-axis represents the value used for the unfolding transition.

We see that the effect of varying k_1 on both F_{un} and x_{pp} is qualitatively the same across all values of f_{01}, increasing both the unfolding force and peak-to-peak distance as previously observed, showing that the f_{ij} parameters do act as scaling factors with respect to the energy term. Again, x_{pp} is not much affected by the variations in f_{01}, but the unfolding force F_{un} shows a significant decrease. It is intuitive to see that, because the multiplication of f_{ij} and ΔE^m_{ij} together are what determine the transition rate, an increase in f_{01} would mean that a smaller E^m_{ij} is required for the same transition probability, and thus a lower unfolding force is observed. However, a more interesting perspective emerges from our observation that f_{ij} relates to something like a mechanical activation energy (see Supporting Information). As $E^m_j < E^m_i$, then increasing f_{ij} reduces the effective mechanical activation energy required to make the transition, thus reducing the unfolding force.

To conclude this investigation, we now investigate the specific behaviour of the FDT model on the same physical system. In this model, we recall that the protein internal force is used to modulate the kinetic transition rates, together with a distance parameter b_{ij}. b_{ij} is a parameter we set in advance, and in principle can be experimentally measured [36, 40], and so we set $b_{ij} = b$, the same for all proteins along the chain. Here we set $k_1 = 30.3$ pN/nm and perform a series of simulations for various

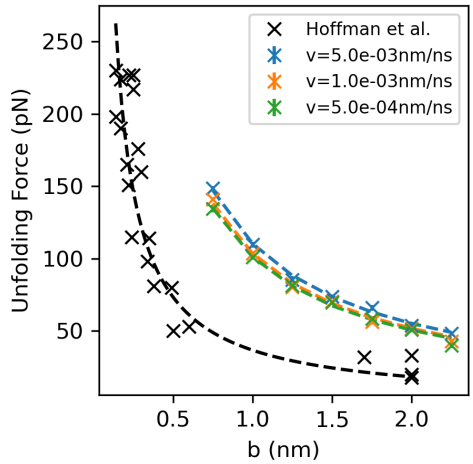

Fig 11. A series of protein unfolding simulations, varying b. We observe a reciprocal dependence of b and the unfolding force, F_{un} both in experimental systems [40] and in our simulations.

values of b and v_c. The results are shown in Fig.11, together with protein unfolding data obtained from the review of Hoffmann *et al.* [40].

We observe a characteristic well-defined reciprocal dependence of unfolding force with the associated distance parameter b. From Hoffmann *et al.* [40], this is indicative of a conserved unfolding energy i.e. a protein may have a higher unfolding force with a lower associated strain, or vice versa, but the multiplication of these two appears to be conserved in nature. In our case, we observe that by setting b in advance, the associated unfolding force F_{un} is returned with a reciprocal dependence on b and, importantly, we can also see the exact dynamic state of the system when unfolding occurs.

To both the experimental data and our simulations, we fit a curve of the form $F_{un}b = E_{ch}$, where E_{ch} is some characteristic energy of unfolding. For Hoffmann *et al.* , we observe $E_{ch} = 36.8 \pm 2.0$pN.nm whereas from our simulations, we calculate $E_{ch} = 110.4 \pm 0.9$pN.nm, 103.6 ± 1.1pN.nm, and 101.2 ± 1.1pN.nm for $v_c = 5 \times 10^{-3}$nm/ns, 1×10^{-3}nm/ns and 5×10^{-4}nm/ns respectively. We observe that the slower the cantilever, the lower the measured value of E_{ch} appears to be. This deviation is completely expected, however, as our simulations are running with significantly higher cantilever speeds v_c compared to experimentally used equipment. As a result, we move to a higher "iso-energy" level compared to Hoffmann *et al.* in Fig.11 as our increased pulling speed overestimates the energy required for the unfolding process. Thus we see that is is not simply the unfolding force that is affected by the speed of the cantilever, but rather the *energy* of unfolding, which is a function of both the unfolding force and in addition, the dynamic relaxation of the system. More discussion on this relaxation is given as Supporting Information.

Conclusions

We have developed a "mechano-kinetic" simulation framework which enables instantaneous kinetic transitions to occur within, and be explicitly affected by, an underlying dynamic simulation framework. We applied this framework to a simple dumbbell simulation to show how we can observe exactly where in phase space kinetic transitions are likely to occur, given a set of experimentally observed mesostate and an

appropriate mechanical model. We have also applied the framework to the case of protein unfolding, and shown how different definitions of "unfolding" i.e. different pairings between the microstates, can yield different behaviours.

The original intention of this project was to develop an empirical framework, enabling the simulation of extremely complex events (i.e. protein unfolding, conformtational changes, binding / unbinding events) to be implicitly simulated in parallel with a dynamic model without the need for extremely high resolution and the large associated amounts of computing power. We believe we have done that, for even though our protein unfolding simulations show deviation from experimental observations, we can still calibrate the model to give the behaviour we desire.

Of course there also exist systems in which the energy barrier between kinetic states is naturally quite low as compared to typical thermal energies: in such cases it is difficult to make a clear distinction between states because transitions between them happen readily and frequently. Intermediate states have been observed in our example systems [36, 49]. The development of Markov state models (MSMs) [50, 51] shows that discrete kinetic states can be defined somewhat arbitrarily, and as such energy barriers can be arbitrarily low. Finally, Bialek *et al.* noted early on that protein dynamics and their reaction rates are coupled [52], such that a majority of the reactive events in some proteins can be coupled to specific protein modes of motion, indicating dynamic specificity. Multiple groups discovered almost in parallel that SMFS-AFM yields different unfolding forces depending on the directions in which you apply force, indicating dynamic anisotropy [53–55]. In these cases, then, the instantaneous location in physical space and associated mechanical energies can have a non-negligible effect on the overall free energies, and thus the transition rates between states. The inspiring work of Trott *et al.* emphasises this, introducing a highly detailed mechanistic model of cytoplasmic dynein which combines a wealth of experimental evidence to deduce the continuous function of the motor [56]. Examination of their computational insights indicates that from an atomistic statistical mechanics perspective, the mesoscopic transition rates emerge from the underlying dynamical behaviour.

Acknowledgments

We would like to thank the group of Professor Lorna Dougan for discussing the work in the context of protein unfolding in complex systems. Ben Hanson was initially supported by the EPSRC through a DTA, and completed the work supported again by the EPSRC with grant EP/P02288X/1 awarded to Professor Lorna Dougan.

References

1. Bates M, Huang B, Rust MJ, Dempsey GT, Wang W, Zhuang X. Sub-Diffraction-Limit Imaging with Stochastic Optical Reconstruction Microscopy. In: A G, R R, J W, editors. Single Molecule Spectroscopy in Chemistry, Physics and Biology. Springer Berlin Heidelberg; 2010.

2. Cheng Y. Single-particle Cryo-EM at crystallographic resolution. Cell. 2015;161(3):450–457. doi:10.1016/j.cell.2015.03.049.

3. Kühlbrandt W. The Resolution Revolution. Science. 2014;343(6178):1443–1444.

4. Frank J. Time-resolved Cryo-Electron Microscopy: Recent Progress. Journal of Structural Biology. 2017;200(3):303–306. doi:10.1016/j.jsb.2017.06.005.Time-resolved.

5. Schermelleh L, Ferrand A, Huser T, Eggeling C, Sauer M, Biehlmaier O, et al. Super-resolution microscopy demystified. Nature Cell Biology. 2019;21(1):72–84. doi:10.1038/s41556-018-0251-8.

6. Lawson CL, Baker ML, Best C, Bi C, Dougherty M, Feng P, et al. EMDataBank.org: Unified data resource for CryoEM. Nucleic Acids Research. 2011;39(SUPPL. 1):456–464. doi:10.1093/nar/gkq880.

7. Solernou A, Hanson BS, Richardson RA, Welch R, Read DJ, Harlen OG, et al. Fluctuating Finite Element Analysis (FFEA): A continuum mechanics software tool for mesoscale simulation of biomolecules. PLoS Computational Biology. 2018;14(3):1–6.

8. Leng J, Shoura M, McLeish TCB, Real AN, Hardey M, McCafferty J, et al. Securing the future of research computing in the biosciences. PLoS Computational Biology. 2019;15(5):1–15. doi:10.1371/journal.pcbi.1006958.

9. Richardson RA, Hanson BS, Read DJ, Harlen OG, Harris SA. Exploring the dynamics of flagellar dynein within the axoneme with Fluctuating Finite Element Analysis. Quarterly Reviews of Biophysics. 2020;53:In press.

10. Hanson BS, Iida S, Read DJ, Harlen OG, Kurisu G, Nakamura H, et al. Continuum mechanical parameterisation of cytoplasmic dynein from atomistic simulation. Methods. 2021;185:39–48. doi:10.1016/j.ymeth.2020.01.021.

11. Kubo S, Li W, Takada S. Allosteric conformational change cascade in cytoplasmic dynein revealed by structure-based molecular simulations. PLoS Computational Biology. 2017;13(9):1–27. doi:10.1371/journal.pcbi.1005748.

12. Reck-peterson SL, Yildiz A, Carter AP, Gennerich A, Vale RD, Mcintosh JR, et al. Single-Molecule Analysis of Dynein Processivity and Stepping Behavior. Cell. 2006;126(2):335–348. doi:10.1016/j.cell.2006.05.046.Single-Molecule.

13. Li L, Alper J, Alexov E. Cytoplasmic dynein binding, run length, and velocity are guided by long-range electrostatic interactions. Scientific Reports. 2016;6(1):1–12. doi:10.1038/srep31523.

14. Kinoshita Y, Kambara T, Nishikawa K, Kaya M, Higuchi H. Step Sizes and Rate Constants of Single-headed Cytoplasmic Dynein Measured with Optical Tweezers. Scientific Reports. 2018;8(1):1–14. doi:10.1038/s41598-018-34549-7.

15. Sasaki K, Kaya M, Higuchi H. A Unified Walking Model for Dimeric Motor Proteins. Biophysical Journal. 2018;115(10):1981–1992. doi:10.1016/j.bpj.2018.09.032.

16. Dudko OK, Hummer G, Szabo A. Intrinsic rates and activation free energies from single-molecule pulling experiments. Physical Review Letters. 2006;96(10):1–4. doi:10.1103/PhysRevLett.96.108101.

17. Na YR, Park C. Investigating protein unfolding kinetics by pulse proteolysis. Protein Science. 2009;18(2):268–276. doi:10.1002/pro.29.

18. West DK, Olmsted PD, Paci E. Mechanical unfolding revisited through a simple but realistic model. Journal of Chemical Physics. 2006;124(15). doi:10.1063/1.2185100.

19. Ohashi KG, Han L, Mentley B, Wang J, Fricks J, Hancock WO. Load-dependent detachment kinetics plays a key role in bidirectional cargo transport by kinesin and dynein. Traffic. 2019;20(4):284–294. doi:10.1111/tra.12639.

20. Belyy V, Schlager MA, Foster H, Reimer AE, Carter AP, Yildiz A. The mammalian dynein-dynactin complex is a strong opponent to kinesin in a tug-of-war competition. Nature Cell Biology. 2016;18(9):1018–1024. doi:10.1038/ncb3393.

21. Linke WA, Ivemeyer M, Mundel P, Stockmeier MR, Kolmerer B. Nature of PEVK-titin elasticity in skeletal muscle. Proceedings of the National Academy of Sciences of the United States of America. 1998;95(14):8052–8057. doi:10.1073/pnas.95.14.8052.

22. Hughes MDG, Cussons S, Mahmoudi N, Brockwell DJ, Dougan L. Single molecule protein stabilisation translates to macromolecular mechanics of a protein network. Soft Matter. 2020;16(27):6389–6399. doi:10.1039/c9sm02484k.

23. Šarlah A, Vilfan A. The winch model can explain both coordinated and uncoordinated stepping of cytoplasmic dynein. Biophysical Journal. 2014;107(3):662–671. doi:10.1016/j.bpj.2014.06.022.

24. Šarlah A, Vilfan A. Minimum requirements for motility of a processive motor protein. PLoS ONE. 2017;12(10):1–13. doi:10.1371/journal.pone.0185948.

25. West DK, Olmsted PD, Paci E. Free energy for protein folding from nonequilibrium simulations using the Jarzynski equality. Journal of Chemical Physics. 2006;125(20):1–7. doi:10.1063/1.2393232.

26. West DK, Paci E, Olmsted PD. Internal protein dynamics shifts the distance to the mechanical transition state. Physical Review E. 2006;74(6):061912.

27. Staple DB, Payne SH, Reddin ALC, Kreuzer HJ. Model for stretching and unfolding the giant multidomain muscle protein using single-molecule force spectroscopy. Physical Review Letters. 2008;101(24):1–4. doi:10.1103/PhysRevLett.101.248301.

28. Sikora M, Sulkowska JI, Witkowski BS, Cieplak M. BSDB: The biomolecule stretching database. Nucleic Acids Research. 2011;39(SUPPL. 1). doi:10.1093/nar/gkq851.

29. Booth JJ, Shalashilin DV. Fully Atomistic Simulations of Protein Unfolding in Low Speed Atomic Force Microscope and Force Clamp Experiments with the Help of Boxed Molecular Dynamics. Journal of Physical Chemistry B. 2016;120(4):700–708. doi:10.1021/acs.jpcb.5b11519.

30. Takada S. Go model revisited. Biophysics and Physicobiology. 2019;16(0):248–255.

31. Bell GI. Models for the specific adhesion of cells to cells. Science. 1978;200(4342):618–627. doi:10.1126/science.347575.

32. Hughes ML, Dougan L. The physics of pulling polyproteins: A review of single molecule force spectroscopy using the AFM to study protein unfolding. Reports on Progress in Physics. 2016;79(7):076601.

33. Imai H, Shima T, Sutoh K, Walker ML, Knight PJ, Kon T, et al. Direct observation shows superposition and large scale flexibility within cytoplasmic dynein motors moving along microtubules. Nature Communications. 2015;6(1):1–11. doi:10.1038/ncomms9179.

34. Kamiya N, Mashimo T, Takano Y, Kon T, Kurisu G, Nakamura H. Elastic properties of dynein motor domain obtained from all-atom molecular dynamics simulations. Protein Engineering, Design and Selection. 2016;29(8):317–326. doi:10.1093/protein/gzw022.

35. Niekamp S, Stuurman N, Zhang N, Vale RD. Three-color single-molecule imaging reveals conformational dynamics of dynein undergoing motility. Proceedings of the National Academy of Sciences of the United States of America. 2021;118(31). doi:10.1073/pnas.2101391118.

36. Bertz M, Rief M. Mechanical Unfoldons as Building Blocks of Maltose-binding Protein. Journal of Molecular Biology. 2008;378(2):447–458. doi:10.1016/j.jmb.2008.02.025.

37. Wood K, Frölich A, Paciaroni A, Moulin M, Härtlein M, Zaccai G, et al. Coincidence of dynamical transitions in a soluble protein and its hydration water: Direct measurements by neutron scattering and MD simulations. Journal of the American Chemical Society. 2008;130(14):4586–4587. doi:10.1021/ja710526r.

38. Telmer PG, Shilton BH. Insights into the Conformational Equilibria of Maltose-binding Protein by Analysis of High Affinity Mutants. Journal of Biological Chemistry. 2003;278(36):34555–34567. doi:10.1074/jbc.M301004200.

39. Hoffmann T, Dougan L. Single molecule force spectroscopy using polyproteins. Chemical Society Reviews. 2012;41(14):4781–4796. doi:10.1039/c2cs35033e.

40. Hoffmann T, Tych KM, Hughes ML, Brockwell DJ, Dougan L. Towards design principles for determining the mechanical stability of proteins. Physical Chemistry Chemical Physics. 2013;15(38):15767–15780. doi:10.1039/c3cp52142g.

41. Tych KM, Hughes ML, Bourke J, Taniguchi Y, Kawakami M, Brockwell DJ, et al. Optimizing the calculation of energy landscape parameters from single-molecule protein unfolding experiments. Physical Review E - Statistical, Nonlinear, and Soft Matter Physics. 2015;91(1):1–9. doi:10.1103/PhysRevE.91.012710.

42. Da Silva MA, Lenton S, Hughes M, Brockwell DJ, Dougan L. Assessing the Potential of Folded Globular Polyproteins As Hydrogel Building Blocks. Biomacromolecules. 2017;18(2):636–646. doi:10.1021/acs.biomac.6b01877.

43. Stirnemann G, Giganti D, Fernandez JM, Berne BJ. Elasticity, structure, and relaxation of extended proteins under force. Proceedings of the National Academy of Sciences of the United States of America. 2013;110(10):3847–3852. doi:10.1073/pnas.1300596110.

44. Zinober RC, Brockwell DJ, Beddard GS, Blake AW, Olmsted PD, Radford SE, et al. Mechanically unfolding proteins: The effect of unfolding history and the supramolecular scaffold. Protein Science. 2009;11(12):2759–2765. doi:10.1110/ps.0224602.

45. Uversky VN. Intrinsically disordered proteins and their "Mysterious" (meta)physics. Frontiers in Physics. 2019;7:8–23. doi:10.3389/fphy.2019.00010.

46. Feller G. Protein stability and enzyme activity at extreme biological temperatures. Journal of Physics Condensed Matter. 2010;22(32). doi:10.1088/0953-8984/22/32/323101.

47. Reed CJ, Lewis H, Trejo E, Winston V, Evilia C. Protein adaptations in archaeal extremophiles. Archaea. 2013;doi:10.1155/2013/373275.

48. Brininger C, Spradlin S, Cobani L, Evilia C. The more adaptive to change, the more likely you are to survive: Protein adaptation in extremophiles. Seminars in Cell and Developmental Biology. 2018;84:158–169. doi:10.1016/j.semcdb.2017.12.016.

49. Isojima H, Iino R, Niitani Y, Noji H, Tomishige M. Direct observation of intermediate states during the stepping motion of kinesin-1. Nature Chemical Biology. 2016;12(4):290–297. doi:10.1038/nchembio.2028.

50. Bowman GR, Pande VS, Noe F. An Introduction to Markov State Models and Their Application to Long Timescale Molecular Simulation. Springer; 2014.

51. Husic BE, Pande VS. Markov State Models: From an Art to a Science. Journal of the American Chemical Society. 2018;140(7):2386–2396. doi:10.1021/jacs.7b12191.

52. Bialek W, Onuchic JN. Protein dynamics and reaction rates: mode-specific chemistry in large molecules? Proceedings of the National Academy of Sciences of the United States of America. 1988;85(16):5908–5912. doi:10.1073/pnas.85.16.5908.

53. Brockwell DJ, Paci E, Zinober RC, Beddard GS, Olmsted PD, Smith DA, et al. Pulling geometry defines the mechanical resistance of a beta-sheet protein. Nature Structural Biology. 2003;10(9):731–737. doi:10.1038/nsb968.

54. Carrion-Vazquez M, Li H, Lu H, Marszalek PE, Oberhauser AF, Fernandez JM. The mechanical stability of ubiquitin is linkage dependent. Nature Structural Biology. 2003;10(9):738–743. doi:10.1038/nsb965.

55. Dietz H, Berkemeier F, Bertz M, Rief M. Anisotropic deformation response of single protein molecules. Proceedings of the National Academy of Sciences of the United States of America. 2006;103(34):12724–12728. doi:10.1073/pnas.0602995103.

56. Trott LE, Hafezparast M, Madzvamuse A. A mathematical understanding of how cytoplasmic dynein walks on microtubules. Royal Society Open Science. 2018;5(8):171568. doi:10.1098/rsos.171568.